Applied Physics Letters

RESEARCH ARTICLE | FEBRUARY 07 2024

Origin of the super-resolution of microsphere-assisted imaging

Alexey V. Maslov ; Vasily N. Astratov

Appl. Phys. Lett. 124, 061105 (2024)
https://doi.org/10.1063/5.0188450

Applied Physics Letters ARTICLE pubs.aip.org/aip/apl

Origin of the super-resolution of microsphere-assisted imaging

Cite as: Appl. Phys. Lett. **124**, 061105 (2024); doi: 10.1063/5.0188450
Submitted: 21 November 2023 · Accepted: 5 January 2024 ·
Published Online: 7 February 2024

View Online Export Citation CrossMark

Alexey V. Maslov[1,a] and Vasily N. Astratov[2]

AFFILIATIONS

[1]Department of Radiophysics, University of Nizhny Novgorod, Nizhny Novgorod 603022, Russia
[2]Department of Physics and Optical Science, University of North Carolina at Charlotte, Charlotte, North Carolina 28233-0001, USA

[a]Author to whom correspondence should be addressed: avmaslov@rf.unn.ru

ABSTRACT

Theoretical explanation of the super-resolution imaging by contact microspheres created a point of attraction for nanoimaging research during the last decade with many models proposed, yet its origin remains largely elusive. Using a classical double slit object, the key factors responsible for this effect are identified by an *ab initio* imaging model comprising object illumination, wave scattering, and image reconstruction from the diffracted far fields. The scattering is found by a full-wave solution of the Maxwell equations. The formation of super-resolved images relies on coherent effects, including the light scattering into the waves circulating inside the microsphere and their re-illumination of the object. Achieving the super-resolution of the double slit requires a wide illumination cone as well as a deeply sub-wavelength object-to-microsphere separation. The resultant image has a significantly better resolution as compared to that from the incoherent imaging theory.

In 2011, it was experimentally demonstrated that a contact dielectric microsphere enables the optical resolution to exceed notably the classical diffraction limit.[1] This has far-reaching practical consequences as microsphere-assisted imaging can become and is already becoming the enabling tool for imaging a broad range of nanoscale objects, for example, plasmonic structures,[1–3] viruses,[4] and computer chips.[5] It can also improve the resolution of existing techniques such as confocal microscopy.[3,6] The limited field-of-view can be widened by translating the microspheres along the samples,[5] stitching the images,[5,7] or using arrays of embedded microspheres.[8,9] Microsphere-assisted imaging is considered as a promising direction of label free imaging along with artificial intelligence, near-field scanning, optical nonlinearity, structured illumination, and optical superlenses and hyperlenses.[10]

While microspheres provide much better resolution than in free space, most attempts to estimate it relied on the discernability of some object features resulting in a wide range of claims, roughly from $\lambda/7$ to $\lambda/17$.[11] However, as noted in Ref. 12, such a procedure can be misleading in general. Fitting experimental images using a convolution with a Gaussian point spread function (PSF) resulted in the resolution value of about $\lambda/7$.[8]

The appearance of the super-resolution enabled by microspheres calls for its explanation. Originally, the super-resolution was attributed to the ability of microspheres to form photonic nanojets and reciprocity of focusing and imaging.[1] However, photonic nanojets are not sufficiently narrow, and reciprocity does not hold if evanescent fields are involved.[11] Still, many studies substitute modeling of imaging by that of focusing. Following the classical imaging theory, the PSF, that is the image of a point source, was calculated[11,13–16] in expectation that its width, which corresponds to resolution, is substantially smaller than the free-space diffraction limit of $\lambda/2$. The best resolution of about $\lambda/4$ was estimated for radially polarized dipoles for which the PSF has a donut-like shape unlike the more common Airy or Gaussian profiles.[14] The possibility of even better resolution, 0.1–0.2λ, for such dipoles was also hypothesized,[17] but the calculated PSF has multiple sidelobes, which are almost as high as the central peak and separated from it by only about twice the width. The excitation of whispering gallery modes (WGMs), a unique property of microspheres, can also provide some narrowing of the PSF, up to $\lambda/4$–$\lambda/3$, but strong sidelobes appear.[11,13,15] In Ref. 18, it was suggested that two nanoparticles with center-to-center distance of 100 nm can be resolved if a WGM is excited, but the image itself resembled interference fringes rather than the two objects. Moreover, the role of WGMs is expected to be rather small for white light illumination used for microsphere-assisted imaging. Several other mechanisms of resolution enhancement have been proposed and studied: conversion of evanescent fields[19,20] (see also topics 25 and 28 in Ref. 10), plasmonics,[14,16] coherent effects,[16,21] and longitudinal modes of microspheres.[22] Contact microspheres may seem similar to solid-immersion lenses (SILs),[23] in which the

resolution enhancement comes from the high index of refraction, which increases the numerical aperture (NA). However, for microspheres, the large-angle waves, which are also required to increase the NA, become trapped inside the microsphere due to the total internal reflection,[24] see Fig. 1(b), and therefore, the NA does not increase. Thus, after 12 years of development, there are still no convincing theoretical demonstrations of the super-resolution at the expected from the experiments level of about $\lambda/7$ and the factors that can contribute to it remain largely speculative.

Here, we demonstrate clearly and unambiguously the super-resolution ability of microsphere-assisted imaging. For this, we adopt an *ab initio* strategy to imaging comprising object illumination, wave scattering, and image reconstruction from the diffracted far fields, see Fig. 1(a). In general, computational methods have become an integral part of microscopy, in particular for imaging sub-wavelength structures,[25] micron-size beads,[26] and microsphere-enhanced interferometry of gratings.[27] Our investigated object is made of two slits with width a and separation b in an infinitely thin perfect metal screen on a substrate with index n_2. The double slit is illuminated from the substrate side, and the transmitted light passes through a microsphere with diameter D separated from the screen by gap d. The light is collected by the microscope objective, which projects it into the sensor array. We consider the Köhler illumination, i.e., mutually incoherent waves originating from different points on the light source. We use 2D geometry and TE polarization with field components $\{E_z, H_x, H_y\}$. Various 2D geometries are common in modeling of imaging.[17,21,27] In our case, this allowed exploring a rather large range of parameters and providing a physical insight into the main effects behind the super-resolution. It is an extremely exhaustive task to complete an analysis comparable to this study in a 3D case, both in terms of software development and subsequent simulations. Yet, our results certainly pave the road to a full 3D implementation.

The modeling procedure is as follows. First, we calculate the scattered fields for each plane wave with fixed α in some range $-\alpha_{max} \le \alpha \le \alpha_{max}$ with increment of 5°. The Maxwell equations are solved by an in-house developed solver based on the frequency-domain finite-integration method. Second, we use $E_z(x,y)$ in the far field region to calculate its spatial spectrum, which can be Fourier transformed to find the corresponding distribution $E_z^b(x,y)$ in any focal plane of the objective by backpropagation.[11,13] The intensity on the sensor array coincides with the intensity in the focal plane except some angular cutoff due to a finite NA of the objective which we take NA = 0.9. This gives the image intensity distribution (partial or coherent image) $I_\alpha(x,y) = |E_z^b(x,y)|^2$ created by a single plane wave incident at α. The x variable in $I_\alpha(x,y)$ is the axial position of the focal plane, and y is the transverse coordinate. Third, we add all partial images $I_\alpha(x,y)$ produced by the plane waves in the specified angular range assuming that the incident light has uniform intensity distribution. This gives us the image distribution $I(x, y)$. The waves with $|\alpha| > 70°$ practically do not contribute to the image formation. The simulation domain has $N_x = 1150$ and $N_y = 1200$ cells in the x and y directions, respectively, with cell size $\Delta x = \Delta y = 10$ nm. The domain is periodic in the y direction and terminated by absorbing layers on both sides along the x axis. In all simulations, we use the following fixed parameters: operating wavelength $\lambda = 600$ nm, microsphere diameter $D = 2R = 5$ μm, double-slit parameters $a = 200$ nm, $b = 70$ nm, and refractive indices $n_1 = 1$, $n_2 = 1.46$ (SiO_2), see Fig. 1(a). All incident waves are assumed to have the same amplitude E_0 and plotted quantities, such as $|E_z(x,y)|$, $I_\alpha(x,y)$, $I(x, y)$, are normalized to $|E_0|$ or to $|E_0|^2$ unless stated otherwise.

We start with free-space imaging, i.e., without microsphere. Figure 2 shows the amplitude $|E_z(x,y)|$ and image $I_\alpha(x,y)$ for the normal $\alpha = 0°$ and oblique $\alpha = 35°$ incidence of a plane wave. In both cases, the field E_z forms a standing wave inside the substrate $x<0$ due to reflection and there is a small leakage through the slits due to diffraction. The images, however, differ significantly. For normal incidence, the image has a single peak centered at the focal plane $x = 0$, making it impossible to distinguish the two slits. For oblique incidence, there are two asymmetric peaks centered at slightly displaced focal planes. Note that for $\alpha = 35°$ the phase fronts along the substrate plane $x = 0$ have a period of $\lambda/(n_2 \sin\alpha) = 716$ nm. A half of this period, which is equivalent to the out-of-phase separation, is 358 nm and comparable to the center-to-center distance of 270 nm between the slits. Thus, to some extent, this is analogous to the emission of out-of-phase currents but with the special scale defined by the wavelength.[16]

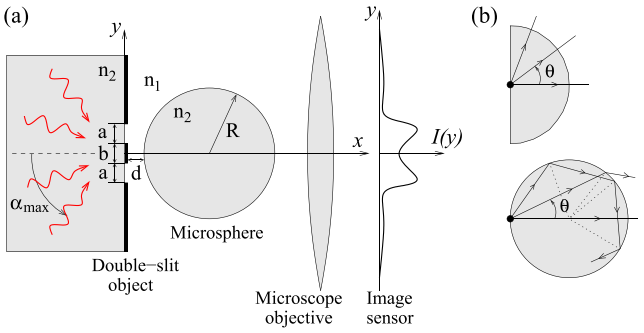

FIG. 1. (a) Schematics of microsphere-assisted imaging of a double slit. (b) Difference in the ray propagation regimes for imaging with a hemispherical SIL and a microsphere.

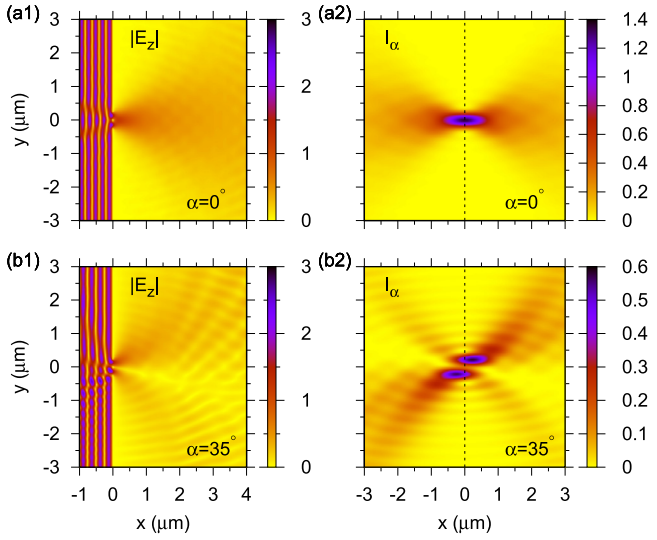

FIG. 2. Distribution of $|E_z(x,y)|$ (left frames) and $I_\alpha(x,y)$ (right frames) for free space imaging for different incident angles: (a1), (a2) $\alpha = 0°$ and (b1), (b2) $\alpha = 35°$. The object planes $x = 0$ in frames (a2) and (b2) are shown by dashed lines.

Figure 3 shows $|E_z(x,y)|$ and $I_\alpha(x,y)$ when a microsphere is located at a deeply subwavelength distance $d = 30$ nm from the double slit. At normal incidence, Figs. 3(a1) and 3(a2), the diffracted light passes through the left boundary of the microsphere and diffracts on the right one. This forms a virtual image to the left of the microsphere. At any focal plane, however, there is no double peak structure that would allow one to identify the double-slit object. At oblique incidence, see Figs. 3(b1) and 3(b2), besides the light refraction at the boundaries of the microsphere, one also observes light trapping, which is not common for the text-book imaging by lenses. The trapping takes place due to the total internal reflection, as illustrated in Fig. 1(b), and the fields inside are weaker than the incident field. The non-resonant nature of this trapping makes it unrelated to the resonant WGM excitation. Such circulating modes can also be excited by point sources[24] or through near-field coupling.[28] The pronounced single peak of I_α observed for $\alpha = 0°$ disappears, and some traces of the double-peak structure develop. The distributions in Figs. 3(c1) and 3(c2) are plotted for a microsphere with an infinitely thin metal obstacle inside which is 600-nm long and oriented vertically. Due to its small size and location, the obstacle affects only the flow of the trapped light just near the boundary since it lies outside the cone defined by the rays that are refracted at 90° at the microsphere surface. Despite the fact that the obstacle scatters only the circulating light, the partial image also changes.

Figure 4 shows the images obtained by summing up all partial images. Figure 4(a) shows $I(x, y)$ with illumination limited by $\alpha_{max} = 70°$ in free space. The two slits are barely discerned due to their deeply subwavelength edge-to-edge separation $b = \lambda/8.6$, see also the curve marked A-FS in Fig. 6. The same slits become clearly resolved if viewed through a microsphere under the same illumination, see Fig. 4(b). The virtual image exists in a rather large range of the focal plane position $-10\,\mu\text{m} \lesssim x \lesssim -5\ \mu\text{m}$, and the largest intensity is at $x = -5.6\ \mu$m. Geometrical optics predicts the virtual image position at $x = -Rn_2/(2 - n_2) \approx -6.8\ \mu$m for $d = 0$. The image formation by the microsphere in Fig. 4(b) requires a large illumination cone $\alpha_{max} = 70°$. If the cone shrinks to

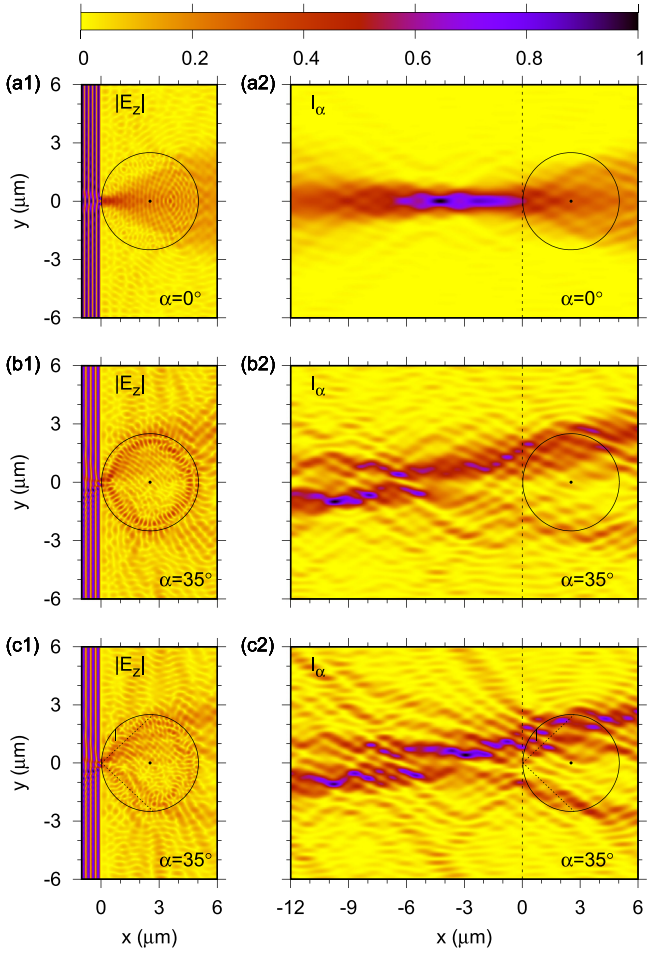

FIG. 3. Distribution of $|E_z(x,y)|$ (left frames) and $I_\alpha(x,y)$ (right frames) for microsphere-assisted imaging for different incident angles: (a1) and (a2) $\alpha = 0°$, (b1, b2, c1, c2) $\alpha = 35°$. In (c1) and (c2) the microsphere has a small metal obstacle near the boundary as shown, and the dotted lines are the rays, which correspond to the critical angle of TIR at the microsphere surface. The centers of the microspheres are marked by black dots, and the object planes are shown by dashed lines. The plotted quantities are normalized to their maximal values: (a1) 2.11, (b1) 2.46, (c1) 2.47, (a2) 0.577, (b2) 0.353, and (c2) 0.330.

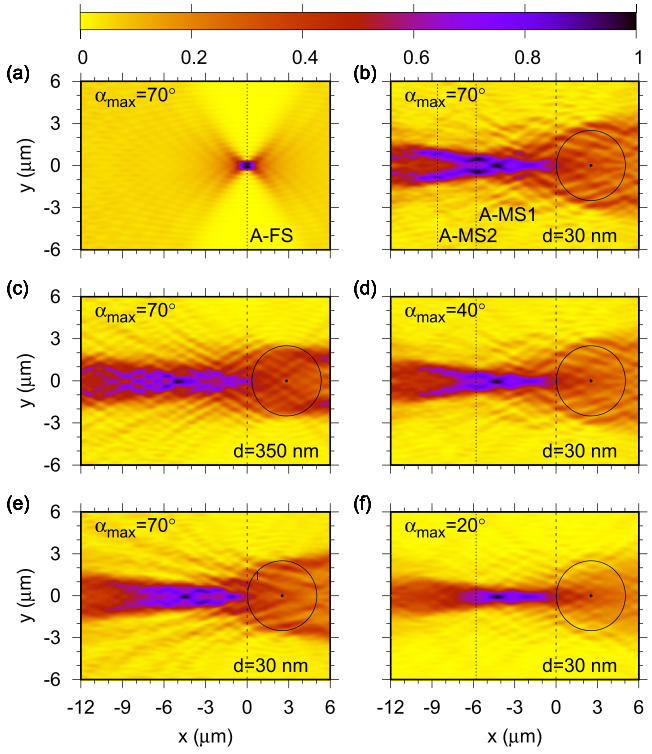

FIG. 4. Images $I(x, y)$: (a) in free space for the maximal angle $\alpha_{max} = 70°$; (b), (d), and (f) with a microsphere for $d = 30$ nm and different values of $\alpha_{max} = 70°$, 40°, 20°, respectively; (c) with a microsphere for $d = 350$ nm and $\alpha_{max} = 70°$; and (e) with a microsphere with a metal obstacle for $d = 30$ nm and $\alpha_{max} = 70°$. The dotted lines labeled A-FS ($x = 0$), A-MS1 ($x = -5.8\ \mu$m), and A-MS2 ($x = -8.6\ \mu$m) show the image planes used in Fig. 6. The object planes are shown by dashed lines. The image intensities are normalized to their maximal values: (a) 12.2, (b) 4.86, (c) 3.55, (d) 4.79, (e) 5.20, and (f) 4.00.

$\alpha_{max} = 20°$, the two slits are unresolved in Fig. 4(f). Increasing α_{max} leads to a continuous development of the image, compare frames (b), (d), and (f) in Fig. 4. The presence of the small metal obstacle, see Fig. 4(e), noticeably deteriorates the image despite the fact that the obstacle affects only the circulating waves at the periphery of the microsphere but not the waves that undergo refraction at its left and right boundaries. This indicates that the circulating light plays a major role in achieving the super-resolution. When the gap increases to $d = 350$ nm (or $\lambda/1.7$), see Fig. 4(c), the image also deteriorates in agreement with experimental observation.[8] Note that the two peaks appearing at $x \approx -3$ μm in the presence of the obstacle, see Fig. 4(e), look similar to the interference ripples in the case of large gap in Fig. 4(c). This similarity can be attributed to the reduction of the circulating light inside the microsphere in both cases. Overall, the smallness of gap provides not only an efficient coupling of light into the microsphere but is also crucial for the re-illumination of the object by the evanescent tails of the circulating light.

Let us now calculate the image using the classical incoherent theory, i.e., by modeling the two slits as two bright stripes, every point of which emits as an independent z-polarized current. This is similar to the model of Ref. 16 in which the emission of coherent currents was compared with that of similarly distributed incoherent sources. The 2D emission problem is solved by using the expansion into the cylindrical functions, and the image is calculated using the same procedure as before. This approach in fact is identical to taking the convolution of the geometrical shape and the PSF. Here, we also account fully for some variation of the PSF since the distance between the microsphere and the point sources on the stripes changes. In this model, the dielectric substrate is removed and the light is collected in the full NA = 1 cone.

Figure 5 shows the incoherent images in free space and with microsphere. The free space image in Fig. 5(a) shows somewhat better resolution as compared to that in Fig. 4(a) as can also be more clearly seen comparing the images at the object plane $x = 0$ labeled A-FS and B-FS in Fig. 6. However, the image with microsphere in Fig. 5(b) is remarkably worse than that in Fig. 4(b), see also images A-MS1, A-MS2, and B-MS in Fig. 6.

Figure 6 compares the images of the two models (*ab initio* and incoherent) in the two regimes (in free space and with microsphere) at several focal planes. Typically, one characterizes the resolution of two incoherent point sources by the depth of the dip in their image, which is equal to 0.735 for the Rayleigh resolution criterion. Here, our object is a double slit, and each slit can be considered as independent only in

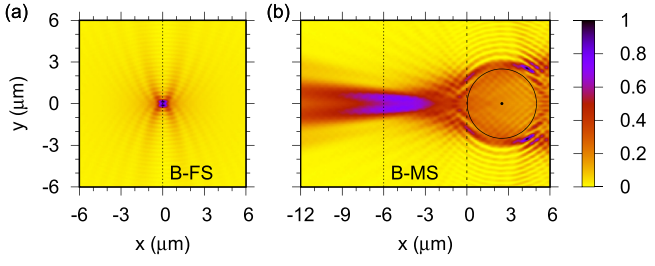

FIG. 5. Incoherent images $I(x, y)$ of two bright stripes (a) in free space and (b) with a microsphere for $d = 30$ nm. The dotted lines labeled B-FS ($x = 0$) and B-MS ($x = -6$ μm) show the image planes used in Fig. 6. The dashed line in frame (b) shows the object plane. The image intensities are normalized to their maximal values.

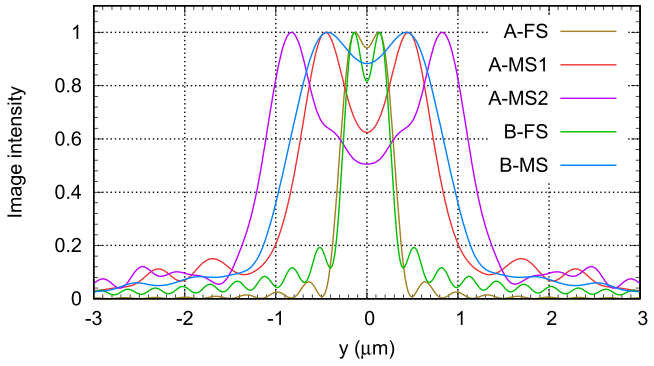

FIG. 6. Comparison of the images $I(x, y)$ at specific focal planes defined by x obtained using different operating regimes (in free space and with microsphere) and models: the *ab initio* model in free space ($x = 0$ for A-FS) and with microsphere ($x = -5.8$ μm for A-MS1 and $x = -8.6$ μm for A-MS2); the incoherent model in free space ($x = 0$ for B-FS) and with microsphere ($x = -6$ μm for B-MS). The corresponding focal planes are shown in Figs. 4(a), 4(b), Figs. 5(a), and 5(b). The images are normalized to their maximal values.

the incoherent approximation. However, from the observer's point of view, we can still attribute higher resolution to the case in which the dip is more pronounced. In free space (A-FS), the slits form two peaks, but the dip between them is very small. The image is slightly better for the incoherent model (B-FS), perhaps due to its higher NA = 1 as compared to NA = 0.9 in the *ab initio* model. The *ab initio* image with the microsphere (A-MS1) clearly has much higher resolution compared to both the free-space (A-FS) and incoherent-model (B-MS) images. The slits are clearly distinguished even if we move the focal plane significantly further away (A-MS2). The peaks at $x = -5.8$ μm (A-MS1) are separated by 0.912 μm and those at $x = -8.6$ μm (A-MS2) by 1.66 μm. Assuming that the centers of the peaks correspond to the centers of the slits, which are separated by 0.27 μm, we obtain magnifications $M \approx 3.4$ and $M \approx 6.1$, respectively. Thus, Fig. 6 clearly shows that the *ab initio* model with the microsphere yields image resolution significantly better compared to that in free space and to that obtained with the microsphere within the framework of incoherent imaging.

Let us now discuss some possible mechanisms of resolution enhancement. The solid immersion provided by microspheres cannot enhance the resolution. Indeed, a hemispherical SIL with index n_2 in free space $n_1 = 1$, see Fig. 1(b), yields NA $= n_2 > 1$ if the full collection angle is used. For a microsphere and the same indices $n_{1,2}$, on the other hand, the rays emitted at θ, for which $n_2 \sin\theta > 1$, are trapped, so the immersion enhancement is completely compensated by the reduction in the angle collection yielding NA = 1 as in free space. The diffraction effects due to finite λ/R reduce the TIR efficiency, yet one can observe quite clearly the trapping of light propagating under large angles, see Figs. 3(b1) and 3(c1). The incoherent model, in fact, correctly accounts for immersion but does not provide any significant resolution enhancement. Indeed, the PSFs for point sources near microspheres are not sufficiently narrow to explain the experimentally observed super-resolution.[13,14,16] The resonant WGMs are not excited, and there is no indication of any relation to photonic nanojets.

Our results suggest that the super-resolution of contact microspheres is associated with coherent scattering of the incident light by

the object into various waves, some of them circulating along the spherical boundary. The trapped light re-illuminates the object with its evanescent tails at almost grazing incidence and also scatters. In the Abbe language, the image is formed by the interference of various diffraction orders, which in microsphere-assisted imaging are produced not only by the direct illumination but also by the coherent light trapped in the microsphere. The interference carries the information about sub-wavelength features of the object that show up as speckles in the partial images, which can be formed if only one plane wave is used for illumination. The broad-angle illumination results in the summation of the partial images yielding an image, which reveals clearly the subwavelength features. The image quality degrades if the light trapping and its re-illumination of the object are hampered by increasing the gap or inserting an obstacle. The results also suggest that large microspheres may not provide such coherent effects because of their large circumference and a finite coherence length for each plane wave component. Due to the importance of coherent scattering, the imaging quality should depend strongly on the type of the object or its features, and therefore, the image may not be described adequately by a single resolution value such as the PSF width. This is the reason why we demonstrated the appearance of the super-resolution by comparing the images with a microsphere and without it but did not attempt to extract any specific value for the resolution. Note that π-shifted current sources produce images with very large resolution at the expense of distortions.[16] Similar effects exist for two π-shifted point sources.[21] Here, instead of using some effective coherent sources, it is shown how coherence arises as the fields get scattered on the double-slit objects. The coherent effects, in general, can cause distortions of sub-wavelength features as, for example, in lithography, where masks have to be deformed to enhance some particular features and achieve the desired intensity distribution on the wafer.[29] The theoretical understanding of the super-resolution mechanisms of microsphere-assisted imaging can also contribute to improving the experimental reliability of this technique.[30]

To conclude, the super-resolution ability of microsphere-assisted imaging has been demonstrated based on the *ab initio* model of imaging. Its origin lies in the coherent effects, including the light scattering into the circulating waves and their re-illumination of the object. Such a regime cannot be described within the framework of the classical incoherent model using the convolution of the PSF and object shape. This highlights the importance of accounting accurately for the wave effects in mesoscale microspheres located at near-field distances from objects with sub-wavelength features.

AVM was supported by the Ministry of Science and Higher Education of the Russian Federation (Grant No. 075-15-2022-293). VNA was supported by the Center for Metamaterials, an NSF I/U CRC, Award No. 1068050. There is no joint funding between the collaborating teams. AVM thanks A. A. Erykalin for early FDTD modeling.

AUTHOR DECLARATIONS

Conflict of Interest

The authors have no conflicts to disclose.

Author Contributions

Alexey Maslov: Conceptualization (lead); Formal analysis (equal); Investigation (lead); Software (lead); Writing – original draft (lead); Writing – review & editing (equal). **Vasily N. Astratov:** Conceptualization (supporting); Formal analysis (equal); Writing – review & editing (equal).

DATA AVAILABILITY

The data that support the findings of this study are available from the corresponding author upon reasonable request.

REFERENCES

[1]Z. Wang, W. Guo, L. Li, B. Luk'yanchuk, A. Khan, Z. Liu, Z. Chen, and M. Hong, "Optical virtual imaging at 50 nm lateral resolution with a white-light nanoscope," Nat. Commun. **2**, 218 (2011).
[2]L. A. Krivitsky, J. J. Wang, Z. Wang, and B. Luk'yanchuk, "Locomotion of microspheres for super-resolution imaging," Sci. Rep. **3**, 3501 (2013).
[3]A. Darafsheh, N. I. Limberopoulos, J. S. Derov, D. E. Walker, Jr., and V. N. Astratov, "Advantages of microsphere-assisted super-resolution imaging technique over solid immersion lens and confocal microscopies," Appl. Phys. Lett. **104**, 061117 (2014).
[4]L. Li, W. Guo, Y. Yan, S. Lee, and T. Wang, "Label-free super-resolution imaging of adenoviruses by submerged microsphere optical nanoscopy," Light **2**, e104 (2013).
[5]F. Wang, L. Liu, H. Yu, Y. Wen, P. Yu, Z. Liu, Y. Wang, and W. J. Li, "Scanning superlens microscopy for non-invasive large field-of-view visible light nanoscale imaging," Nat. Commun. **7**, 13748 (2016).
[6]Y. Yan, L. Li, C. Feng, W. Guo, S. Lee, and M. Hong, "Microsphere-coupled scanning laser confocal nanoscope for sub-diffraction-limited imaging at 25 nm lateral resolution in the visible spectrum," ACS Nano **8**, 1809–1816 (2014).
[7]B. Jin, A. R. Jean, A. V. Maslov, and V. N. Astratov, "Ball lens-assisted cellphone imaging with submicron resolution," Laser Photonics Rev. **17**, 2300146 (2023).
[8]K. W. Allen, N. Farahi, Y. Li, N. I. Limberopoulos, D. E. Walker, Jr., A. M. Urbas, V. Liberman, and V. N. Astratov, "Super-resolution microscopy by movable thin-films with embedded microspheres: Resolution analysis," Ann. Phys. **527**, 513–522 (2015).
[9]A. Brettin, F. Abolmaali, K. F. Blanchette, C. L. McGinnis, Y. E. Nesmelov, N. I. Limberopoulos, D. E. Walker, Jr., I. Anisimov, A. M. Urbas, L. Poffo, A. V. Maslov, and V. N. Astratov, "Enhancement of resolution in microspherical nanoscopy by coupling of fluorescent objects to plasmonic metasurfaces," Appl. Phys. Lett. **114**, 131101 (2019).
[10]V. N. Astratov, Y. B. Sahel, Y. C. Eldar, L. Huang, A. Ozcan, N. Zheludev, J. Zhao, Z. Burns, Z. Liu, E. Narimanov, N. Goswami, G. Popescu, E. Pfitzner, P. Kukura, Y.-T. Hsiao, C.-L. Hsieh, B. Abbey, A. Diaspro, A. LeGratiet, P. Bianchini, N. T. Shaked, B. Simon, N. Verrier, M. Debailleul, O. Haeberle, S. Wang, M. Liu, Y. Bai, J.-X. Cheng, B. S. Kariman, K. Fujita, M. Sinvani, Z. Zalevsky, X. Li, G.-J. Huang, S.-W. Chu, O. Tzang, D. Hershkovitz, O. Cheshnovsky, M. J. Huttunen, S. G. Stanciu, V. N. Smolyaninova, I. I. Smolyaninov, U. Leonhardt, S. Sahebdivan, Z. Wang, B. Luk'yanchuk, L. Wu, A. V. Maslov, B. Jin, C. R. Simovski, S. Perrin, P. Montgomery, and S. Lecler, "Roadmap on label-free super-resolution imaging," Laser Photonics Rev. **17**, 2200029 (2023).
[11]A. V. Maslov and V. N. Astratov, "Resolution and reciprocity in microspherical nanoscopy: Point-spread function versus photonic nanojets," Phys. Rev. Appl. **11**, 064004 (2019).
[12]C. J. R. Sheppard, "Resolution and super-resolution," Microsc. Res. Tech. **80**, 590–598 (2017).
[13]Y. Duan, G. Barbastathis, and B. Zhang, "Classical imaging theory of a microlens with super-resolution," Opt. Lett. **38**, 2988–2990 (2013).
[14]V. M. Sundaram and S.-B. Wen, "Analysis of deep sub-micron resolution in microsphere based imaging," Appl. Phys. Lett. **105**, 204102 (2014).
[15]T. X. Hoang, Y. Duan, X. Chen, and G. Barbastathis, "Focusing and imaging in microsphere-based microscopy," Opt. Express **23**, 12337–12353 (2015).
[16]A. V. Maslov and V. N. Astratov, "Imaging of sub-wavelength structures radiating coherently near microspheres," Appl. Phys. Lett. **108**, 051104 (2016).
[17]R. Heydarian and C. R. Simovski, "Non-resonant subwavelength imaging by dielectric microparticles," Photonics Nanostruct. **46**, 100950 (2021).

[18]S. Zhou, Y. Deng, W. Zhou, M. Yu, H. P. Urbach, and Y. Wu, "Effects of whispering gallery mode in microsphere super-resolution imaging," Appl. Phys. B **123**, 236 (2017).
[19]Y. Ben-Aryeh, "Increase of resolution by use of microspheres related to complex Snell's law," J. Opt. Soc. Am. A **33**, 2284–2288 (2016).
[20]R. Boudoukha, S. Perrin, A. Demagh, P. Montgomery, N.-E. Demagh, and S. Lecler, "Near- to far-field coupling of evanescent waves by glass microspheres," Photonics **8**, 73 (2021).
[21]S. Perrin, R. Pierron, P. Gerard, P. Montgomery, and S. Lecler, "Miniaturized microsphere-assisted microscopy," Appl. Phys. Lett. **122**, 161108 (2023).
[22]A. R. Bekirov, B. S. Luk'yanchuk, and A. A. Fedyanin, "Virtual image within a transparent dielectric sphere," JETP Lett. **112**, 341–345 (2020).
[23]S. M. Mansfield and G. S. Kino, "Solid immersion microscope," Appl. Phys. Lett. **57**, 2615–2616 (1990).
[24]A. V. Maslov, B. Jin, and V. N. Astratov, "Wave optics of imaging with contact ball lenses," Sci. Rep. **13**, 6688 (2023).
[25]M. Totzeck and H. J. Tiziani, "Interference microscopy of sub-λ structures: A rigorous computation method and measurements," Opt. Commun. **136**, 61–74 (1997).
[26]I. R. Çapoğlu, C. A. White, J. D. Rogers, H. Subramanian, A. Taflove, and V. Backman, "Numerical simulation of partially coherent broadband optical imaging using the finite-difference time-domain method," Opt. Lett. **36**, 1596–1598 (2011).
[27]T. Pahl, L. Hüser, S. Hagemeier, and P. Lehmann, "FEM-based modeling of microsphere-enhanced interferometry," Light **3**, 699–711 (2022).
[28]A. V. Kanaev, V. N. Astratov, and W. Cai, "Optical coupling at a distance between detuned spherical cavities," Appl. Phys. Lett. **88**, 111111 (2006).
[29]C. A. Mack, *Field Guide to Optical Lithography* (SPIE Press, Bellingham, WA, 2006).
[30]R. Malureanu, O. Takayama, E. Shkondin, A. Novitsky, and A. V. Lavrinenko, "Microspherical nanoscopy: Is it a reliable technique?" OSA Continuum **3**, 10–19 (2020).